

## RESEARCH LETTER

10.1002/2014GL062016

## Key Points:

- We analyzed ambient noise records from 206 stations in Korea, China, and Japan
- Group velocity maps were created in the period range of 10 to 70 s
- Low group velocity anomalies in the Ulleung Basin are found at long periods

## Correspondence to:

M. Witek,  
mwitek@earth.northwestern.edu

## Citation:

Witek, M., S. van der Lee, and T.-S. Kang (2014), Rayleigh wave group velocity distributions for East Asia using ambient seismic noise, *Geophys. Res. Lett.*, 41, 8045–8052, doi:10.1002/2014GL062016.

Received 25 SEP 2014

Accepted 3 NOV 2014

Accepted article online 6 NOV 2014

Published online 24 NOV 2014

## Rayleigh wave group velocity distributions for East Asia using ambient seismic noise

Michael Witek<sup>1</sup>, Suzan van der Lee<sup>1</sup>, and Tae-Seob Kang<sup>2</sup>

<sup>1</sup>Department of Earth and Planetary Sciences, Northwestern University, Evanston, Illinois, USA, <sup>2</sup>Department of Earth and Environmental Sciences, Pukyong National University, Busan, South Korea

**Abstract** Vertical component data from 206 broadband seismometer stations from Korean networks Korean Institute of Geoscience and Mineral Resources and Korea Meteorological Administration, the Japanese F-net network, and the Chinese New China Digital Seismograph Network and Northeast China Extended Seismic Array network are collected for the year 2011, and the ambient seismic noise is analyzed. Rayleigh wave group velocity distribution maps are created in the period range 10 to 70 s. Our results are largely consistent with previous studies of the area but provide greater detail in the Korean peninsula and the Sea of Japan. Low group velocities are observed in the Ulleung basin, and the Chubu-Kanto and Kyushu regions in Japan. At 10 s period, sediment basins in the Sea of Japan appear as low group velocity regions relative to higher group velocity continental regions. At periods longer than 40 s, a low group velocity region emerges in the Ulleung basin region, and is bounded by the Korean peninsula.

## 1. Introduction

Ambient seismic noise analysis is now an established method for producing tomographic models in regions of low seismic activity. Laboratory experiments have shown that one can estimate the Green's function for the medium between a pair of receivers, assuming a diffuse wavefield (i.e., random wave phases and azimuthally isotropic and spatially homogeneous wavefield) [Lobkis and Weaver, 2001]. Although the ambient seismic wavefield is not diffuse [Mulargia, 2012], group and phase velocity dispersion curves extracted from the noise are consistent with similar measurements made using earthquake signals [Shapiro *et al.*, 2005], suggesting that a fully diffuse field is not a requirement for ambient noise tomography.

The Korean peninsula has a relatively low rate of seismic activity, and earthquakes with magnitudes  $M_w > 4.0$  occur less than once per year on the Korean peninsula [Choi *et al.*, 2009]. Such a low occurrence rate makes it difficult to perform a high-resolution regional study of the crust and upper mantle using earthquake data. Thus, the Korean peninsula presents a prime region for ambient seismic noise analysis.

Seismic velocity models derived from ambient seismic noise analysis have been produced for various locations around the world [e.g., Moschetti *et al.*, 2007; Lin *et al.*, 2007; Liang and Langston, 2008; Bensen *et al.*, 2009; Yang *et al.*, 2010]. While models have been produced for the greater East Asian region [e.g., Zheng *et al.*, 2011], none incorporate data from the Korean broadband seismometer networks operated by the Korea Meteorological Administration (KMA) and the Korean Institute of Geoscience and Mineral Resources (KIGAM). Other studies including KMA and KIGAM data have either used accelerograph stations which limit the analysis to relatively high frequencies, i.e.,  $> 0.15$  Hz [Choi *et al.*, 2009; Kang and Shin, 2006], or have included KMA broadband stations in conjunction with accelerograph stations [Cho *et al.*, 2007] to extend the analysis to the period range 0.5 to 20 s.

Here we produce high-resolution Rayleigh wave group velocity maps of the region. A map of the study region is provided in Figure 1. Using 88 stations from the Northeast China Extended Seismic Array (NECES-Array) in Northeast China, four stations from the New China Digital Seismograph Network (IC), 19 stations from the KMA network, 21 stations from the KIGAM network, and 74 stations from the Japanese F-net network, we have produced Rayleigh wave dispersion curve maps in the period range of 10 to 70 s.

## 2. Data Processing

We collected vertical component data at 1 sample per second from 206 broadband seismometer stations in Korea, Japan, and China for the year 2011. Each station's data had their instrument responses removed and

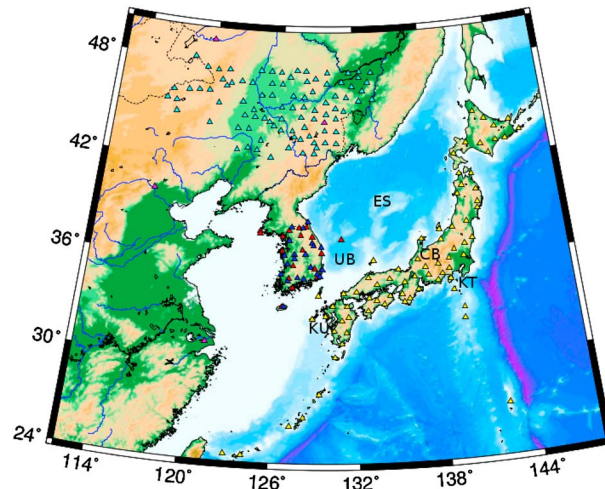


**Figure 1.** Map of the stations used in this study. Included are 19 KMA stations (red), 21 KIGAM stations (blue), 4 IC stations (purple), 74 F-net stations (yellow), and 88 NECESSArray stations (cyan). Abbreviations are as follows: ES: Sea of Japan; UB: Ulleung Basin; CB: Chubu; KT: Kanto; KU: Kyushu.

FTN method over the running-absolute-mean method of *Bensen et al.* [2007] because we find that the FTN method generally produces cross correlations with larger signal-to-noise ratios (SNRs). We define the SNR to be the ratio of the maximum amplitude in a signal window to the RMS of a 500 s long trailing noise window, 2000 s after the signal window. The signal window is defined by the arrival times for surface waves traveling at 2 and 5 km/s for a particular station pair.

After normalization, each unique pair of stations have their respective 24 h time series cross correlated and stacked. Usually, the entire data set is cross correlated and stacked, as it has been shown that the cross correlation approximates the Green's function of the medium between the receiver pair as the cross-correlation window increases. However, to estimate the errors in the measured group velocities we choose multiple sets of 90 random days to cross correlate and stack. In Figure 2,

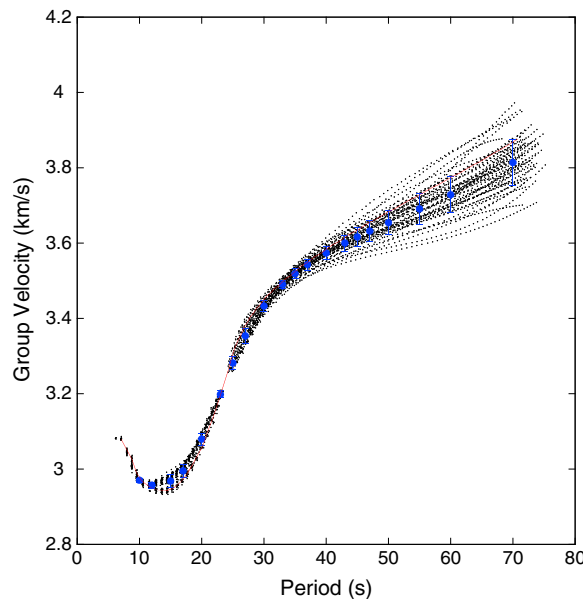


**Figure 2.** Dispersion curve measurement for the KMA station pair BAR and DAG2. The black dots are dispersion curve measurements made on 90 random days chosen out of the year 2011. The blue points are the mean dispersion curve with associated standard deviations for error bars. The red curve is a dispersion curve measured for a full 1 year stack.

were merged in one time series in order to resolve timing issues. In order to efficiently cross-correlate 2 yearlong time series, the merged time series were cut into 24 h chunks which were detrended. Large amplitude events, such as earthquakes, can overwhelm seismic surface wave signals in the ambient noise. Therefore, to down-weight large amplitude signals, as well as to simulate the diffuse wavefield requirement of equipartitioned modes, the time series must be processed in a step referred to as normalization. Each 24 h chunk was normalized using the frequency-time normalization (FTN) method described by *Shen et al.* [2012]. In short, the FTN method works by subjecting a seismogram to a series of narrow band-pass filters, dividing each filtered time series by its envelope, and finally summing the individual filtered and normalized time series. We choose to use the

FTN method over the running-absolute-mean method of *Bensen et al.* [2007] because we find that the FTN method generally produces cross correlations with larger signal-to-noise ratios (SNRs). We define the SNR to be the ratio of the maximum amplitude in a signal window to the RMS of a 500 s long trailing noise window, 2000 s after the signal window. The signal window is defined by the arrival times for surface waves traveling at 2 and 5 km/s for a particular station pair.

*Zeng and Ni* [2010] noted interference in their Green's function approximations from Rayleigh waves generated by a strong, persistent microseismic source located on the Japanese island of Kyushu. Ignoring this deviation from the assumption of a diffuse field could result in a systematic overestimation of Rayleigh wave group velocities. The location of this signal was reaffirmed by *Zheng et al.* [2011], and it was attributed to volcanic tremors at Aso volcano [*Takagi et al.*, 2009]. To assess the effect of the Kyushu microseism on our data set, we replicate

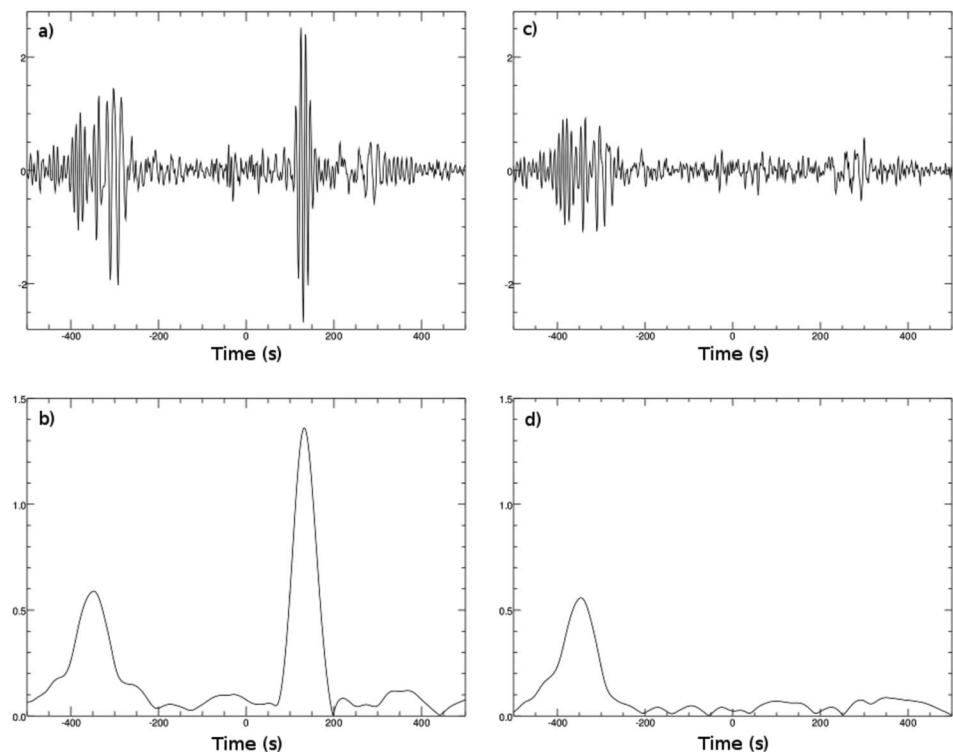


**Figure 3.** Cross correlations (CC) between stations SSE and INCN. (a) Raw 2 year stack of CCs for years 2007 to 2009. (b) Envelope of (a) filtered between 10 and 12 s period. (c) Raw 1 year CC stack for the year 2011. (d) Envelope of Figure 3c filtered between 10 and 12 s period. The Kyushu microseism is seen to be active during the time period 2007–2009, but not for the year 2011. The signals here were retrieved using the FTN method. Compared with the results of Zheng *et al.* [2011], the FTN method produces results consistent with RAM.

the observations of Zheng *et al.* [2011] by cross correlating the same 2 years of data (2007–2009) for stations INCN and SSE, and we compare it to a 1 year stack for the year 2011 (Figure 3). Evidently, the Kyushu microseism does not appear to have much of an effect for the year 2011. Record sections of F-net stations cross correlated with all other stations are also missing the Kyushu microseism signal. We thus conclude that for our data set, the Kyushu microseismic signal is below the noise level and should not have an effect on our resulting dispersion curve measurements. By comparing cross-correlations before and after the 2011 Tohoku earthquake, we also find that the 2011 Tohoku earthquake and its aftershocks do not significantly alter our measurements.

Before dispersion curve measurement, quality control is performed in a multistep process. We find a useful statistic to be the correlation coefficient (CC),

$$CC_{xy} = \frac{\sum_i^N x_i y_i}{\sqrt{\sum_i^N x_i^2 \sum_i^N y_i^2}}, \tag{1}$$

which is simply the covariance of two signals  $x$  and  $y$  divided by the product of their standard deviations. For two perfectly correlated signals,  $CC = 1$ , while two perfectly anticorrelated signals will have a  $CC = -1$ .

Most studies use the so-called symmetric signal, which is the average of the negative (“acausal”) and positive (“causal”) lag time sides of the cross correlation, with the natural assumption that the Green’s function is equal for both time directions. In this case, the symmetric signal should at least have the same SNR as both causal and acausal sides without any loss of information. However, in the presence of an asymmetric noise source distribution, we find that averaging the acausal and causal sides of the cross correlation may result in a decrease in SNR in different frequency bands. Should the symmetric operation result in a higher SNR, the acausal and causal sides of the cross correlation will be in phase and the corresponding CC for the two sides will be greater than zero.

We measure the CC on the causal side of the cross correlation with respect to the acausal side, in their respective signal windows. By plotting a 2-D histogram of the CC versus the SNR after the symmetric operation, we have chosen a conservative threshold value of 0.5 for separating those cross correlations whose signals in the causal and acausal sides are in phase and therefore result in a high SNR after averaging the two, from those cross correlations which are highly asymmetric and averaging results in a lower SNR. For those cross correlations with a CC value less than 0.5, we measured the dispersion curve on the side with the higher SNR, with the assumption that it represents the dominant direction of ambient seismic energy propagation. Likewise, if the CC is greater than 0.5, then the dispersion curve is measured on the symmetric signal. During dispersion curve measurement, should any SNR be found to be less than 10, that measurement is discarded. Furthermore, we disregarded measurements at periods for which the interstation distance is smaller than three wavelengths.

To measure the group velocities, we follow the method of *Bensen et al.* [2007]. A series of Gaussian filters are applied to the analytic signal, with center frequencies from 5 s to 100 s, in steps of 1 s period. The group velocities are measured by finding the lag time of the maximum amplitude of the filtered signal and then dividing the interstation distance by the measured lag time. The frequency of the measurement is taken to be the instantaneous frequency, which is the time derivative of the phase at the measured lag time. This is used because, when the spectrum of the signal is not flat, the central frequency of the Gaussian filter will not accurately represent the frequency of the output [*Bracewell, 1978*].

### 3. Surface Wave Tomography

Each group velocity dispersion curve can be estimated to represent an average along the path between the corresponding station pair. We construct a spherical shell of 10,041 grid nodes separated by 0.3° on average. The grid nodes are derived through triangular tessellation of a sphere, as described by *Wang and Dahlen* [1995] and used in Moho depth parameterization by *van der Lee and Nolet* [1997]. The dispersion curves are regionalized by setting up an inverse problem in which we obtain the group velocity value needed at each node in order to give the average group velocity measured along each path, for every period. In other words, each row of our design matrix  $\mathbf{G}$  is a set of coefficients derived through trilinear interpolation that relate each station-station great circle path to the appropriate grid nodes. The inverse problem is solved using a Python implementation of the LSMR routine of *Fong and Saunders* [2011]. LSMR is an iterative method for solving least squares problems similar to the well-known LSQR method [*Paige and Saunders, 1982*] but has been shown to converge sooner. Essentially, we are minimizing a misfit equation defined to be

$$\Phi(\vec{m}) = \left( \mathbf{G}\vec{m} - \vec{d} \right)^T \mathbf{C}_e^{-1} \left( \mathbf{G}\vec{m} - \vec{d} \right) + \lambda_f^2 \|\mathbf{F}\vec{m}\|^2 + \lambda_D^2 \|\mathbf{I}\vec{m}\|^2, \quad (2)$$

where  $\mathbf{G}$  is the design matrix relating the data vector  $\vec{d}$  to the values at the model nodes of  $\vec{m}$ ,  $\mathbf{C}_e^{-1}$  is the inverse of the data covariance matrix (in this case a diagonal matrix of the measured uncertainties),  $\mathbf{F}$  is a flattening matrix representing a discretized version of the first derivative operator, and  $\mathbf{I}$  is the identity matrix. The  $\lambda$  values are scalars representing the strength of the flattening and damping. The values for the  $\lambda$  are chosen by plotting tradeoff curves of model complexity versus fit to the data. We construct  $\vec{d}$  to be differences between our measured group velocities and the group velocities predicted by *iasp91* [*Kennett and Engdahl, 1991*]. The model vector  $\vec{m}$  then represents perturbations with respect to the *iasp91* group velocity dispersion curve at every grid node. The final group velocity distribution maps are created by adding the *iasp91* group velocity dispersion curve to  $\vec{m}$ . The solution for  $\vec{m}$  in the least squares sense is

$$\vec{m} = \left( \mathbf{G}^T \mathbf{C}_e^{-1} \mathbf{G} + \lambda_f^2 \mathbf{F}^T \mathbf{F} + \lambda_D^2 \right)^{-1} \mathbf{G}^T \mathbf{C}_e^{-1} \vec{d}. \quad (3)$$

The large size and underdetermined nature of our inverse problem makes a quantitative estimate of the model errors not feasible. To estimate the reliability of the final models, we perform resolution testing by creating hypothetical Gaussian checkerboard models. We calculate a synthetic data vector by multiplying  $\mathbf{G}$  by the hypothetical model. To the synthetic data is added Gaussian noise scaled to the norm of the measured uncertainties. The synthetic data are then inverted, and the results at 20 s period are shown in Figure 4. In regions of low-data coverage, anomalies are smeared out along the dominant direction of the raypaths. This can be seen in the northern portion of the Sea of Japan, and this effect becomes worse as the size of the anomalies decreases. However, despite the relatively poor raypath coverage, larger size anomalies (e.g., 5° × 5°) are retrieved fairly well, indicating that the large-scale features seen in our models are

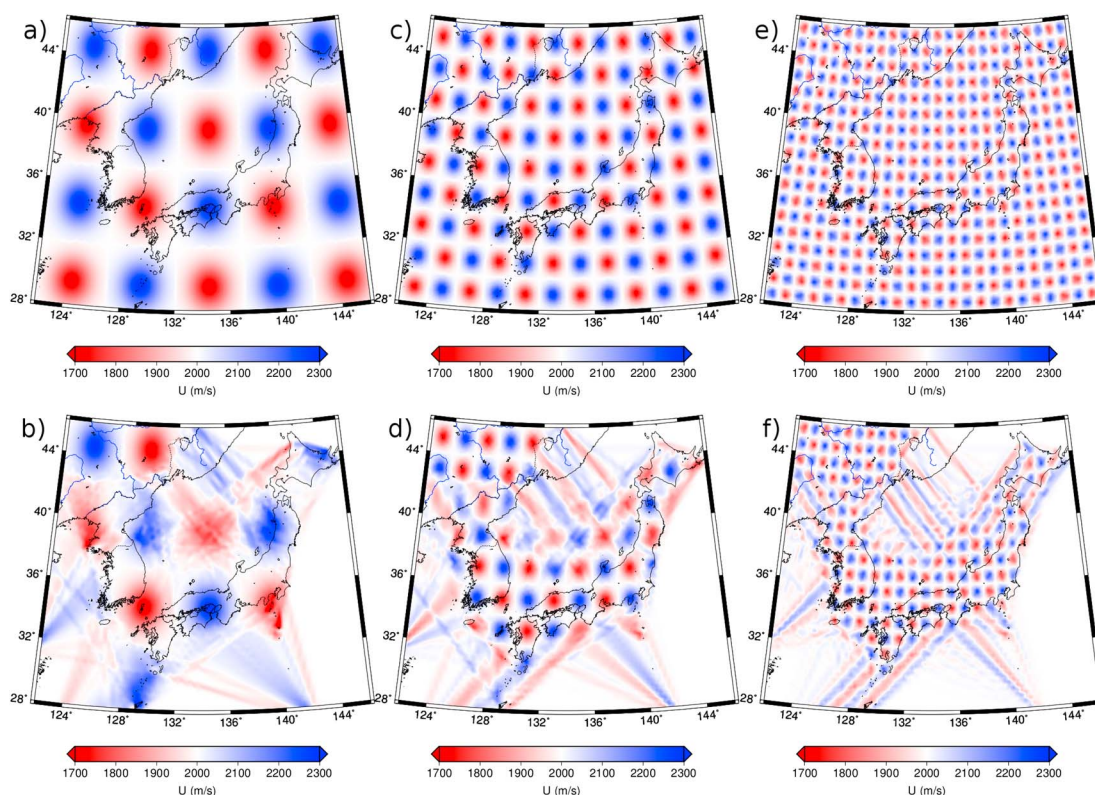


**Figure 4.** Resolution test at 20 s period for Gaussian anomalies of three different sizes. Gaussian anomalies of  $\pm 300$  m/s are added to a flat background velocity of 2 km/s. (a and b) The input model and retrieved model, respectively, for anomalies of size  $5^\circ \times 5^\circ$ . Likewise, (c and d) anomalies of size  $2^\circ \times 2^\circ$  and (e and f) anomalies of size  $1^\circ \times 1^\circ$ .

robust. Elsewhere in the model, the Korean peninsula, the southern portion of the Sea of Japan, and Japan are resolved very well.

To find portions of the region with inadequate data coverage, we attempt to retrieve a uniform model at each period. A hypothetical model is created with a constant background velocity of 2.05 km/s. A synthetic data vector is created for each period by multiplying  $\mathbf{G}$  by the flat background model. After the addition of Gaussian noise to the synthetic data, the data are inverted and the result is compared with the flat background model. Regions of the retrieved model where the amplitudes are less than or equal to  $\pm 0.5\%$  of the flat background model are then used as masks for the group velocity distribution maps.

#### 4. Results

Figure 5 shows group velocity distribution maps at periods of 10, 20, 30, 40, 50, and 70 s. At 10 s period, low-velocity anomalies are prominent in the Sea of Japan, as the existence of a water layer and deep sedimentary basins will effectively lower group velocities. On continental crusts, the 10 s Rayleigh wave is most sensitive to middle crustal structures, and so we observe higher velocities in Korea and Japan in contrast with sediment basins in the Sea of Japan. At 20 s period, we begin to see the dichotomy between continental and oceanic crusts. Because oceanic crust is thinner, Rayleigh waves at the same period sample higher mantle speeds, as opposed to thicker continental crust, which is relatively slower. Previous studies [e.g., Lee *et al.*, 1999; Kim *et al.*, 2003] have shown that crust in the Sea of Japan is thicker than usual oceanic crust, and this agrees with our observations where we begin to see higher speeds in the Sea of Japan at longer periods ( $> 15$  s).

At periods of around 30 s, Rayleigh waves are sensitive to contrasts in shear wave speeds above and below the Moho discontinuity, and thus, we observe low-velocity anomalies in Japan where previous studies [e.g., Nishida *et al.*, 2008; Zhao *et al.*, 1992] have shown thicker than usual crust. Relative to speeds in Korea, we can infer that Japanese crust should be thicker than that in Korea, which is in agreement with previous studies of Moho depth in Korea from teleseismic receiver function analysis [e.g., Chang and Baag, 2007].

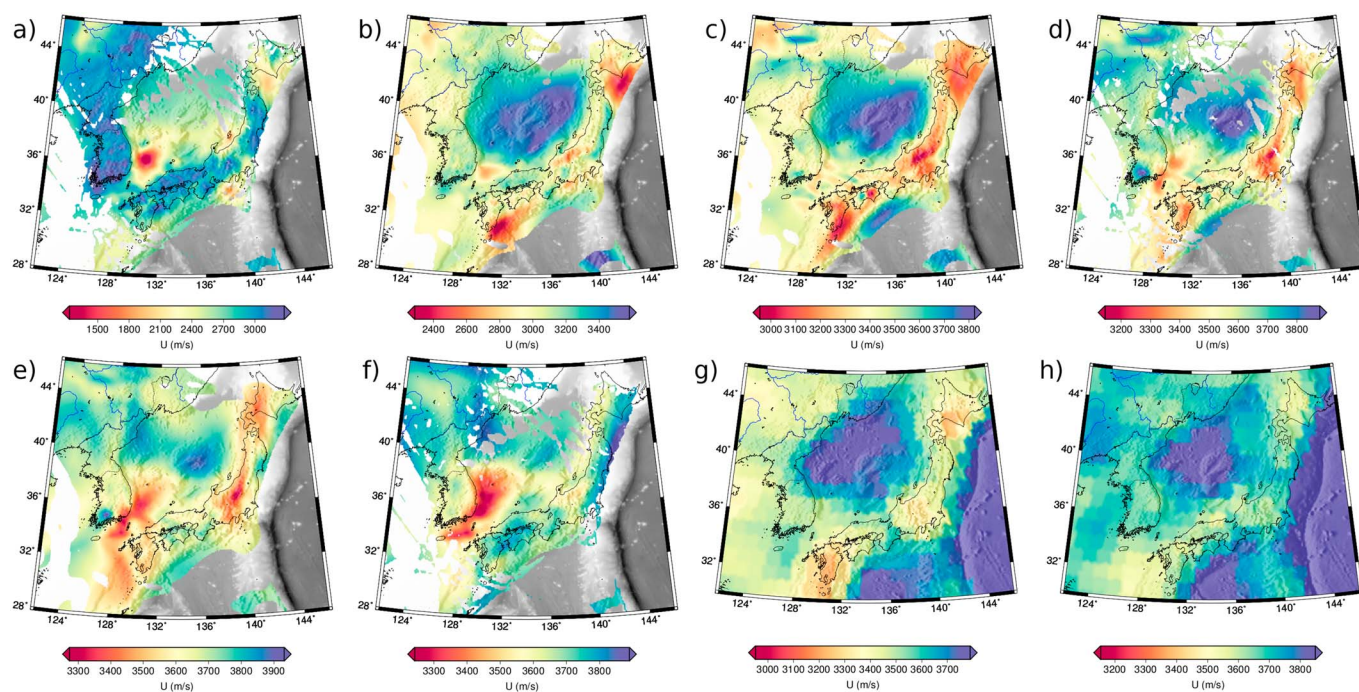


**Figure 5.** Maps of Rayleigh wave group velocity distributions at (a) 10, (b) 20, (c) 30, (d) 40, (e) 50, and (f) 70 s period. (g and h) Predicted group velocity maps at periods of 30 and 40 s period, respectively, from the LITHO1.0 model of *Pasyanos et al.* [2014].

At longer periods ( $> 40$  s), we still observe the same low-velocity anomaly in Japan, and we begin to observe the emergence of a low-velocity anomaly in the Ulleung basin region, which is bounded by the Korean peninsula. In Figure 5, we also show Rayleigh wave group velocity distribution predictions at periods of 30 and 40 s, derived from the LITHO1.0 model [*Pasyanos et al.*, 2014]. The LITHO1.0 model is a  $1^\circ$  tessellated model of the crust and upper mantle, constructed by perturbing initial models to fit high-resolution Rayleigh and Love wave dispersion maps in the period range 25 to 200 s. Compared to our results, the 30 s map predicts low-velocity anomalies in roughly the same regions, but not as low as we have mapped. The 40 s map differs from our results, missing the low-velocity anomaly of the Ulleung Basin, and the high-velocity anomaly in the southwestern Korean peninsula. These differences may be attributed to the increase in local resolving power as a result of the addition of KMA and KIGAM data.

In Japan, the low-velocity anomaly at 40 s period is possibly due to the effects of partial melting occurring above the subducting Pacific slab. As long-period Rayleigh waves are sensitive to variations in lithospheric properties, the low-velocity anomaly in the Ulleung Basin region may be due to a contrast in the properties of the lithosphere in the Sino-Korean craton and the lithosphere underneath the Sea of Japan and may be attributable to a hotter than normal mantle below the Ulleung Basin. *Horozal et al.* [2009] used the depth to clathrates in the 20 Ma old Ulleung Basin as an indicator of temperature. Relatively high temperatures suggest heat flows above  $105 \text{ mW/m}^2$ , which are high for a basin of this age. *Kim et al.* [2003] analyzed multichannel seismic reflection and ocean bottom seismometer data across the Korean margin into the Ulleung Basin and inferred the existence of a high  $P$  wave velocity layer ( $7.1\text{--}7.4 \text{ km/s}$ ) under the eastern coast of Korea. They interpret this as evidence for magmatic underplating as a result of high upper mantle temperatures. However, despite there being several lines of evidence for higher than normal upper mantle temperatures, the complexity of interpreting Rayleigh wave group velocity sensitivity kernels somewhat obfuscates the origins of the group velocity anomalies. Future work will determine the 3-D seismic velocity structure of the region using this data set.

## 5. Conclusions

Using 1 year of continuous broadband seismic data at 206 stations across Korea, China, and Japan, we have derived 21,115 Rayleigh wave group velocity dispersion curves and estimated their uncertainties. Using these measured dispersion curves, we have performed surface wave tomography to produce Rayleigh wave

group velocity distribution maps in the period range 10 to 70 s. At 10 s period, we observe low velocities in the Sea of Japan in contrast with higher continental crust velocities. The low velocities are due to the water layer, with prominent low-velocity regions corresponding with sedimentary basins, such as the Ulleung basin. At periods longer than 20 s, the Sea of Japan is observed as a high-velocity region relative to continental regions, due to the thinness of oceanic-type crust. At periods of 30 to 40 s, low velocities in the Chubu-Kanto regions indicate thicker crust than in the Korea peninsula. At periods of 40 to 50 s, low velocities in the Chubu-Kanto regions may be a result of partial melting above the subducting Pacific slab. From 40 to 70 s period, we observe the emergence of a prominent low-velocity region underneath the Ulleung basin, bounded by the Korean peninsula, which may be a remnant of higher than normal mantle temperatures associated with the rifting of the southwestern portion of the Sea of Japan. Further work will be aimed at completing a point-by-point inversion of the group velocity maps to retrieve the Moho depth and a 1-D velocity profile at each grid node.

### Acknowledgments

F-net data are obtainable from the National Research Institute for Earth Science and Disaster Prevention in Japan, and New China Digital Seismograph Network and Northeast China Extended Seismic Array data are available through the facilities of the IRIS Data Management System. Data from the Korea Meteorological Administration and the Korea Institute of Geoscience and Mineral Resources are obtainable upon request (<http://www.kma.go.kr>, <http://www.kigam.re.kr/>). We thank each agency for collecting and distributing the data. This work began under a National Science Foundation East Asia and Pacific Summer Institutes Fellowship and has been funded by the Air Force Research Laboratory under award number FA9453-11-C-0231, and by the Korea Meteorological Administration Research and Development Program under grant CATER 2012-5051. Maps were plotted using Generic Mapping Tools. We would like to thank two anonymous reviewers for providing constructive feedback of the manuscript. Special thanks go to Robert Langan for providing GPU enabled desktop computers for data processing.

Eric Calais thanks Anatoli Levshin and one anonymous reviewer for their assistance in evaluating this paper.

### References

- Bensen, G. D., M. H. Ritzwoller, M. P. Barmin, A. L. Levshin, F. Lin, M. P. Moschetti, N. M. Shapiro, and Y. Yang (2007), Processing seismic ambient noise data to obtain reliable broad-band surface wave dispersion measurements, *Geophys. J. Int.*, *169*(3), 1239–1260, doi:10.1111/j.1365-246X.2007.03374.x.
- Bensen, G. D., M. H. Ritzwoller, and Y. Yang (2009), A 3-D shear velocity model of the crust and uppermost mantle beneath the United States from ambient seismic noise, *Geophys. J. Int.*, *177*, 1177–1196, doi:10.1111/j.1365-246X.2009.04125.x.
- Bracewell, R. N. (Ed.) (1978), *The Fourier Transform and Its Applications*, McGraw-Hill Book Co., New York.
- Chang, S.-J., and C.-E. Baag (2007), Moho depth and crustal  $v_p/v_s$  variation in southern Korea from teleseismic receiver functions: Implication for tectonic affinity between the Korean Peninsula and China, *Bull. Seismol. Soc. Am.*, *97*(5), 1621–1631, doi:10.1785/0120050264.
- Cho, K. H., R. B. Hermann, C. J. Ammon, and K. Lee (2007), Imaging the upper crust of the Korean peninsula by surface-wave tomography, *Bull. Seismol. Soc. Am.*, *97*(1B), 198–207, doi:10.1785/0120060096.
- Choi, J., T.-S. Kang, and C.-E. Baag (2009), Three-dimensional surface wave tomography for the upper crustal velocity structure of southern Korea using seismic noise correlations, *Geosci. J.*, *13*(4), 423–432, doi:10.1007/s12303-009-0040-2.
- Fong, D. C.-L., and M. Saunders (2011), LSMR: An iterative algorithm for sparse least-squares problems, *SIAM J. Sci. Comput.*, *33*(5), 2950–2971, doi:10.1137/10079687X.
- Horozal, S., G. H. Lee, B. Y. Yi, D. G. Yoo, K. P. Park, H. Y. Lee, W. Kim, H. J. Kim, and K. Lee (2009), Seismic indicators of gas hydrate and associated gas in the Ulleung Basin, East Sea (Japan Sea) and implications of heat flows derived from depths of the bottom-simulating reflector, *Mar. Geol.*, *258*, 126–138, doi:10.1016/j.margeo.2008.12.004.
- Kang, T.-S., and J. S. Shin (2006), Surface-wave tomography from ambient seismic noise of accelerograph networks in southern Korea, *Geophys. Res. Lett.*, *33*, L17303, doi:10.1029/2006GL027044.
- Kennett, B. L. N., and E. R. Engdahl (1991), Traveltimes for global earthquake location and phase identification, *Geophys. J. Int.*, *105*(2), 429–465, doi:10.1111/j.1365-246X.1991.tb06724.x.
- Kim, H.-J., H.-T. Jou, H.-M. Cho, H. Bijwaard, T. Sato, J.-K. Hong, H.-S. Yoo, and C.-E. Baag (2003), Crustal structure of the continental margin of Korea in the East Sea (Japan Sea) from deep seismic sounding data: Evidence for rifting affected by the hotter than normal mantle, *Tectonophysics*, *364*(1–2), 25–42, doi:10.1016/S0040-1951(03)00048-9.
- Lee, G. H., H. J. Kim, M. C. Suh, and J. K. Hong (1999), Crustal structure, volcanism, and opening mode of the Ulleung Basin, East Sea (Sea of Japan), *Tectonophysics*, *308*, 503–525, doi:10.1016/S0040-1951(99)001113-4.
- Liang, C., and C. A. Langston (2008), Ambient seismic noise tomography and structure of eastern North America, *J. Geophys. Res.*, *113*, B03309, doi:10.1029/2007JB005350.
- Lin, F.-C., M. H. Ritzwoller, J. Townend, and S. Bannister (2007), Ambient noise Rayleigh wave tomography of New Zealand, *Geophys. J. Int.*, *170*(2), 649–666, doi:10.1111/j.1365-246X.2007.03414.x.
- Lobkis, O. I., and R. L. Weaver (2001), On the emergence of the Green's function in the correlations of a diffuse field, *J. Acoust. Soc. Am.*, *110*(6), 3011–3017, doi:10.1121/1.1417528.
- Moschetti, M. P., M. H. Ritzwoller, and N. M. Shapiro (2007), Surface wave tomography of the western United States from ambient seismic noise: Rayleigh wave group velocity maps, *Geochem. Geophys. Geosyst.*, *8*, Q08010, doi:10.1029/2007GC001655.
- Mulargia, F. (2012), The seismic noise wavefield is not diffuse, *J. Acoust. Soc. Am.*, *131*, 2853–2858, doi:10.1121/1.3689551.
- Nishida, K., H. Kawakatsu, and K. Obaru (2008), Three-dimensional crustal S wave velocity structure in Japan using microseismic data recorded by Hi-net tiltmeters, *J. Geophys. Res.*, *113*, B10302, doi:10.1029/2007JB005395.
- Paige, C. C., and M. A. Saunders (1982), LSQR: An algorithm for sparse linear equations and sparse least squares, *ACM Transactions on Mathematical Software (TOMS)*, *8*(1), 43–71, doi:10.1145/355984.355989.
- Pasyanos, M. E., T. G. Masters, G. Laske, and Z. Ma (2014), LITHO1.0: An updated crust and lithospheric model of the Earth, *J. Geophys. Res. Solid Earth*, *119*, 2153–2173, doi:10.1002/2013JB010626.
- Shapiro, N. M., M. Campillo, L. Stehly, and M. H. Ritzwoller (2005), High-resolution surface-wave tomography from ambient seismic noise, *Science*, *307*, 1615–1618, doi:10.1126/science.1108339.
- Shen, Y., Y. Ren, and H. Gao (2012), An improved method to extract very-broadband empirical Green's functions from ambient seismic noise, *Bull. Seismol. Soc. Am.*, *102*(4), 1872–1877, doi:10.1785/0120120023.
- Takagi, N., S. Kaneshima, T. Ohkura, M. Yamamoto, and H. Kawakatsu (2009), Long-term variation of the shallow tremor sources at Aso volcano from 1999 to 2003, *J. Volcanol. Geotherm. Res.*, *184*(3), 333–346, doi:10.1016/j.jvolgeores.2009.04.013.
- van der Lee, S., and G. Nolet (1997), Upper mantle S velocity structure of North America, *J. Geophys. Res.*, *102*(B10), 22,815–22,838, doi:10.1029/97JB01168.
- Wang, Z., and F. A. Dahlen (1995), Spherical-spline parameterization of three-dimensional Earth models, *Geophys. Res. Lett.*, *22*, 3099–3102, doi:10.1029/95GL03080.
- Yang, Y., et al. (2010), Rayleigh wave phase velocity maps of Tibet and the surrounding regions from ambient seismic noise tomography, *Geochem. Geophys. Geosyst.*, *11*, Q08010, doi:10.1029/2010GC003119.

- Zeng, X., and S. Ni (2010), A persistent localized microseismic source near Kyushu Island, Japan, *Geophys. Res. Lett.*, *37*, L24307, doi:10.1029/2010GL045774.
- Zhao, D., S. Horiuchi, and A. Hasegawa (1992), Seismic velocity structure of the crust beneath the Japan islands, *Tectonophysics*, *212*(3–4), 289–301, doi:10.1016/0040-1951(92)90296-I.
- Zheng, Y., W. Shen, L. Zhou, Y. Yang, Z. Xie, and M. H. Ritzwoller (2011), Crust and uppermost mantle beneath the North China Craton, northeastern China, and the Sea of Japan from ambient noise tomography, *J. Geophys. Res.*, *116*, B12312, doi:10.1029/2011JB008637.